

Numerical Simulation of Dual-Mode Scramjet Combustors

C.G. Rodriguez
National Research Council

NA61-2167

D.W. Riggins
University of Tennessee at Knoxville

1N-07

R.D. Bittner
FDC/NYMA, Inc.
NASA Langley Research Center

Abstract

Results of a numerical investigation of a three-dimensional dual-mode scramjet isolator-combustor flow-field are presented. Specifically, the effect of wall cooling on upstream interaction and flow-structure is examined for a case assuming jet-to-jet symmetry within the combustor. Comparisons are made with available experimental wall pressures. The full half-duct for the isolator-combustor is then modeled in order to study the influence of side-walls. Large scale three-dimensionality is observed in the flow with massive separation forward on the side-walls of the duct. A brief review of convergence-acceleration techniques useful in dual-mode simulations is presented, followed by recommendations regarding the development of a reliable and unambiguous experimental data base for guiding CFD code assessments in this area.

Introduction

This paper presents the results of several ongoing computational fluid dynamics (CFD) studies related to dual-mode scramjet operation. The focus of these numerical studies is to:

- i) select candidate experimental flow-fields which are amenable to numerical modeling,
- ii) identify issues related to the accurate modeling of these flow-fields,
- iii) develop convergence-acceleration techniques for the dual-mode problem, and
- iv) make recommendations for a well-posed experimental investigation.

Previous work in the simulation of dual-mode scramjet combustors has identified shortcomings in the current ability to accurately model both the extent of the upstream interaction and the details of the pressure distribution in the combustor (Riggins, 1998).

Specifically, the extent of upstream interaction was underpredicted in that reference by approximately 30% and peak wall pressure was overpredicted by approximately 15% for a selected experimental configuration. It was believed at the conclusion of this preliminary study that these discrepancies were primarily due to turbulence modeling issues and three-dimensional effects occurring in the experiment (unable to be captured by the CFD which relied on piece-wise symmetry). This particular experimental configuration has since been studied extensively using several different CFD codes with more advanced turbulence modeling and solvers; some of these results will be reviewed in this paper. They include specific studies of wall-temperature effects on upstream interaction, and three-dimensional effects in dual-mode flow-fields.

The first section describes the main physical characteristics of the flow-field of a scramjet in dual-mode operation. The second section details recent modeling activity on a dual-mode experiment performed in Japan. Convergence-acceleration techniques useful to dual-mode simulations are identified and discussed in the third section. The fourth section makes recommendations for the level and type of experimental data necessary to provide an adequate data-base for improving CFD simulations of dual-mode flow-fields. The last section provides a summary of the work and conclusions presented in the paper.

1.0 Characteristics of Dual-Mode Combustion

The dual-mode scramjet is characterized by interaction of the heat-release in the combustor with the flow-field upstream of the fuel-injection region, i.e., the flow pressurizes upstream of the combustor. This is similar to ramjets with Kantrowitz-Donaldson internal inlets. In such inlets, the flow is dominated by a normal shock downstream of the inlet throat. Due to the choked nozzle-throat downstream of the combustor, changes in heat-release (i.e., throttling) mandates changes in the location of the inlet normal-shock: too much heat-release will move the shock upstream to the inlet physical throat and rapidly out of the inlet, resulting in unstart.

In the case of a high-speed scramjet combustor (flight Mach above 8), the ratio of inflow total-enthalpy to downstream heat-release is sufficiently high so that the combustion-generated pressure-rise is confined to the combustor (i.e., downstream of the fuel-injection region). As flight Mach is lowered, the ratio drops and the combustor flow-field begins to interact with the upstream flow-field. This situation is inherently transitional between a ram-mode and a scram-mode of operation, and is hence termed as dual-mode.

Although the ratio of inflow-enthalpy to downstream heat-release is important in determining whether upstream interaction can occur, other factors have also been identified as critical drivers for the extent and shape of the upstream interaction region (Anderson et al, 1977; McClinton, 1978; Eggers et al, 1978): inflow distortion, non-adiabatic conditions, step-changes in flow, downstream expansion ration, etc.

In order to avoid inlet unstart in the mid-speed regime, three techniques are commonly used. First, combustor-area increases in the form of backward-facing steps or downstream expansions have the effect of decreasing the onset and extent of upstream interaction. Sec-

ond, axially-staged injection is used so that combustion is localized and controlled to some extent. Third, a constant-area duct is added between the combustor and the inlet; such a component, termed the isolator, 'isolates' the combustor interaction from the inlet and hence provides buffering from unstart.

The upstream interaction in a dual-mode flow-field is typified by the development of large recirculation bubbles well into the isolator, with an oblique-shock train embedded between the bubbles (see Figure 1). The flow-field in the isolator-combustor for dual-mode operation is complex and highly variable; the core flow can be entirely subsonic or remain supersonic. Broad features of the flow are driven by relatively small effects such as incoming boundary-layer characteristics. Due to the large recirculation bubbles present in the flow, three-dimensional characteristics can be significant and coupling of these recirculation regions with walls and corner-flows can cause significant lateral distortion.

Because of system and weight issues, it is advantageous to have as small an isolator as possible consistent with the mission-requirements of the dual-mode scramjet engine. This mandates the need for robust prediction capability for the flow-fields within the isolator-combustor during dual-mode operation. Well-known correlations have been developed from one-dimensional and two-dimensional flow analysis (Billig et al, 1969; Billig et al, 1972; Waltrup and Billig, 1973a, 1973b); these correlations are based on such parameters as incoming boundary-layer thickness (critical for determining the onset of separation) and maximum combustor-to-inflow pressure. They perform well on simple model geometries (axi-symmetric or two-dimensional), but are not suitable for more complex three-dimensional problems except for providing directions and trends.

Recent computational modeling of three-dimensional dual-mode scramjet combustor has been reported in Riggins (1998), Mizobuchi et al (1997), and Matsuo et al (1998), which focus on an experiment performed in Japan. These numerical studies demonstrated the ability of three-dimensional CFD to capture the qualitative features of the upstream interaction, but also identified modeling issues which prevented quantitative agreement with the available data. Therefore, the purpose of the present paper will be to describe ongoing efforts to improve the predictive capability of fully-elliptic three-dimensional solvers necessary for the dual-mode scramjet combustor.

2.0 Three-Dimensional Dual-Mode Flow-Field Investigation

2.1 Description of Experiment

The experiment modeled in this numerical investigation was performed at the National Aerospace Laboratory in Japan and is extensively documented in a number of references (Komuro et al, 1990; Murakami et al, 1993; Chinzei et al, 1998). This experiment was originally selected for a preliminary CFD investigation which was reported in Riggins (1998). A brief summary of the experiment is as follows: a vitiated air heater provides Mach 2.5 inflow (representing a flight condition of Mach 7.5) to a isolator-combustor as shown in Figure 2. Note that the facility nozzle has its expansion direction matched to the combustor width rather than its height; this may introduce issues related to inflow distur-

tion. Small backward-facing steps (height 0.32 cm) are located on top and bottom walls at the combustor-entrance section. The isolator extends 0.22 meters upstream of the combustor entrance. At the end of the combustor (0.096 meters downstream from steps) both top and bottom wall expand at 1.7 degrees. The entire geometry is of constant width (0.1473 meters), and the combustor height before steps is 0.032 meters. Fuel injection occurs 0.013 meters downstream from steps. There are five equally-spaced fuel-injector orifices on the bottom wall, with spacing between injectors set at 0.032 meters. There are four fuel-injectors located on the top wall (interdigitated with respect to the bottom injectors). Hydrogen fuel-injection is sonic and normal to the combustor walls. The diameters of the two side injector orifices on the bottom row are reduced such that one-half of the mass flow rate of hydrogen is injected (relative to the main injectors). Experimental wall-pressures are available on the duct centerline from isolator entrance (facility-nozzle exit) to downstream expansion section. A number of cases were run in the experiment with varying degree of upstream interaction, ranging from tare (no fuel injection) to a fuel equivalence-ratio ϕ of 1.0 (maximum upstream interaction), as well as varying total temperature. Cases examined numerically include the fuel equivalence-ratios of 1.0 and 0.8 at a total temperature of 2000 Kelvin. Both cases demonstrate significant upstream interaction in terms of wall pressure. Original CFD on this experiment (Mizobuchi et al, 1997; Matsuo et al, 1998) used adiabatic walls; however subsequent information has suggested that a wall temperature of about 500 Kelvin would be appropriate. Both conditions are examined in this work.

Inflow (nominal) conditions:

• Mach	2.5
• Total pressure	1.0 MPa
• Total temperature	2000 Kelvin
• Mass-fraction O ₂	0.24335
• Mass-fraction N ₂	0.5835
• Mass-fraction H ₂ O	0.17315

Injection conditions:

• Mach	1.0
• Total temperature	280 Kelvin
• Discharge coefficient	0.85 (approximate)
• Equivalence ratio	0.80/1.0

2.2 Computational Method

Riggins (1998) used a full Navier-Stokes solver derived from the original SPARK code at NASA LaRC. The turbulence model employed was a $k-\omega$ (Menter's baseline model) two-equation model (Menter, 1992). As previously noted, wall-pressures were overpredicted and upstream interaction distance underpredicted using this code. Jet-to-jet symmetry was

assumed for this preliminary study due to resource availability. The ongoing work reported on here has involved the use of the LaRC code VULCAN (White and Morrison, 1999), which is an elliptic Navier-Stokes upwind finite-volume CFD code. It has a number of turbulence models available; again, Menter's $k-\omega$ model was used extensively in this ongoing investigation. Near-wall behavior is modeled using Wilcox' wall-matching approach (Wilcox, 1998). Wilcox' compressibility corrections are also used (Wilcox, 1998). Full finite-rate chemical-kinetics are available in this code; for this investigation a 7-species, 7-reaction model (Drummond et al, 1991) was used, as well as a global one-step model with arbitrary coefficients to ensure complete reaction.

2.3 Results

The three-dimensional facility-nozzle was modeled in a separate preliminary effort from nozzle inlet to nozzle exit (isolator entrance) in order to provide accurate inflow conditions to the isolator/combustor simulation. Two different domains are considered in this work. The first domain extends from jet-centerline to jet-centerline with the assumption of lateral symmetry as made in earlier CFD investigations. The second domain spanned the half-duct with symmetry assumed only on the duct centerline and allows a comparative study regarding three-dimensional effects.

2.3.1 Jet-to-Jet Modeling

The grid for this case is as follows: isolator - $201(\text{axial}) \times 41(\text{lateral}) \times 29(\text{vertical})$; combustor and expansion-region - $277(\text{axial}) \times 41(\text{lateral}) \times 45(\text{vertical})$. In this case and all subsequent jet-to-jet symmetry cases, the incoming flow for the isolator was simply stripped-off as a 2-D slice from the larger simulation of the full three-dimensional facility-nozzle, i.e. there is no lateral variation of the inflow for the isolator-combustor. All cases presented were run with the 7-species, 7-reaction chemistry model.

As to the boundary-conditions, the inflow was imposed from the nozzle calculation, as explained above; the exit boundary was a supersonic extrapolation. The bottom-wall was modeled as no-slip, either adiabatic or isothermal (see below). The top boundary corresponds to the horizontal center-plane and was modeled as anti-symmetric (see Figure 2). Finally, the two side boundaries were represented as symmetric.

1) Adiabatic wall

Figure 3 shows predicted Mach contours on the duct centerline for the adiabatic-wall, $\phi = 1.0$ case when jet-to-jet symmetry is assumed (in this figure and in Figure 5, vertical scale is twice the horizontal scale for better visualization of the flow-field). This figure demonstrates the significant degree of upstream interaction which occurs at this high fuel equivalence-ratio case. Note that fuel injection occurs slightly downstream of the $x = 0$ location. The injection and subsequent reaction-induced pressurization feeds upstream through the mechanisms of large subsonic recirculation zones on both top and bottom walls. A series of oblique shocks forms in the core flow within the isolator, and between the upper and lower recirculation-bubbles. The extent of upstream interaction is predicted at about 4.5 isolator heights upstream of the step. There is an oblique shock-train established in the

isolator with the core Mach dropping to just above 1.0 in the vicinity of the steps. Note that the previous CFD reported in Riggins (1998) showed entirely high subsonic flow in the vicinity of the steps and injectors; the current simulation demonstrates in contrast a (low Mach number) supersonic core.

Wall pressure on the bottom jet centerline is shown in Figure 4. Both predicted and experimental wall pressures are in good agreement in terms of the extent of upstream interaction. This is an improvement over the 30% underprediction reported in Riggins (1998). However, peak wall pressure in the vicinity of the injection is still overpredicted by approximately 15% (similar to the over-prediction reported in the same reference). Note that the same turbulence models were used in both simulations, as well as the same chemistry-model. However, the previous work used an approximate nozzle in order to generate the inflow to the isolator, whereas the work reported here used an exact representation of the nozzle geometry to generate the inflow profile.

Figure 4 includes two different grid sequences: fine (which corresponds to the actual grid), and medium (which differs from the fine by a factor of 2 in each computational coordinate); this is part of the grid-sequencing acceleration-technique described later in this paper. At present, there is no significant difference between the wall pressures for the two grids. Work is still in progress to determine grid sensitivity and convergence.

2) Isothermal wall

This solution uses the same turbulence model, and kinetics mechanism as the previous, adiabatic, case; however, calculations so far were done on the medium sequence only. The previous adiabatic-wall, medium-sequence solution was used as initial condition. Figure 5 is a plot of predicted Mach contours on the duct (bottom jet) centerline for a constant wall-temperature of 500 Kelvin. The leading-edge of the oblique shock-train remains at about the same axial location. However, the strength of the shocks are visibly increased; in fact, the core-flow is driven fully subsonic in the downstream (combustor) region. Note that there are a number of interpretations for this effect. First, cooling of the flow results in a de-energized boundary-layer which may result in greater separation (recall that cooling the near-wall subsonic flow results in lower velocity). The stronger shock structure observed can also result from a higher Mach-number at the leading edge of the separation bubble (i.e. where the supersonic outer-edge of the core flow impinges and turns over the bubble) (recall that cooling a supersonic flow increases Mach number of that flow). Essentially, the thinner boundary-layer means that supersonic flow encounters the leading-edge of the separation-bubble nearer to the wall, resulting in a greater turning-angle. Another possible bulk effect is the cooling of the separation bubbles themselves (large subsonic regions) tend to increase local pressures and decrease local velocities. It is intriguing that cooling this flow has such an impact on extent of the upstream pressure rise as seen in Figure 6 and that the trend is clearly of increased pressure with cooling, counter to one-dimensional reasoning. The importance of upstream 3-D modeling is clearly evident as the shock-structure/separated-zone dynamics are complex and not predictable without adequate modeling and adequate boundary and inflow information.

There are some concerns that the transient-path taken (i.e. beginning a simulation using the isothermal condition from an initial-condition corresponding to the adiabatic-case solution) could be a factor in the final flow-field obtained. This has not been observed to be a significant issue at this time, although investigation is continuing.

2.3.2 Half-Duct Modeling

Ongoing studies of this experiment include numerical modeling of the entire half-width of the duct. Experimental fuel contours obtained by probe transverses on downstream crossflow planes indicate considerable three-dimensionality to the flow, with high concentrations of fuel toward the duct centerline and almost no fuel near the side walls of the duct. Results obtained so far correspond to a one-step chemistry model, for convergence-acceleration purposes (see below).

The grid used for the duct was: isolator - 101(axial) \times 101(width) \times 29(height); combustor and expansion-region - 141(axial) \times 101(width) \times 45(height).

The inflow boundary-condition was interpolated from the nozzle calculation, the center-plane boundary was assumed symmetric, and the exit was set as extrapolation. The top, bottom and side walls were all modeled as no-slip, isothermal with a temperature of 500 Kelvin.

1) $\phi = 1.0$

For the base-line of fuel equivalence-ratio 1.0, the numerical simulation of the flow-field indicated massive lateral non-uniformity in the duct. Specifically, the upstream interaction extended all the way into the facility nozzle on the sidewall; the front of the separated zone then angled back to the centerline of the duct, with the upstream-interaction distance at the centerline closely matching the experiment. A large separation bubble was observed to form on the sidewall and merged with the separated zones on top and bottom walls. Because the numerical simulation assumes a fixed nozzle-outflow, the solution for this high fuel equivalence-ratio case could only be viewed as evidence for the three-dimensionality of the flow; duct centerline pressure traces and upstream interaction distances can be very misleading in terms of actual isolator performance.

2) $\phi = 0.8$

In order to attempt to capture the complete extent of the upstream interaction, a case is currently being examined with a fuel equivalence ratio of 0.8. This case has somewhat less upstream interaction, as evidenced by centerline experimental pressure-traces. A view of the Mach contours looking from the front top of the domain is shown in Figure 7. In this figure, the centerline symmetry-plane is at the back, top-wall is above, bottom-wall below, and side-wall is nearest to the viewer. The strong upstream displacement of the recirculation region at the sidewall is evident; this region extends downstream at an angle in the lateral direction towards the recirculation bubble located at the duct centerline. The upstream interaction at the side-wall is still very close to the nozzle exit (isolator entrance). The

large recirculation zone associated with the side-wall and the top and bottom recirculation zones can be seen in this figure.

Figure 8 is a view of fuel contours on downstream crossflow planes from the CFD. There is an unambiguous movement of the fuel toward the sidewalls, counter to experimental measurements which indicate fuel moving toward the centerline of the duct. One possibility which has been raised is that there may be overpressurization of the combustor with respect to the static pressure at the (presumably sonic) fuel orifices. This could result in a problematic redistribution of fuel mass flow-rate from the injector arrays (note that the outboard fuel injectors are reduced in diameter). This effect would not be captured by the CFD at the current level of modeling, which assumes even mass flow rate distributions across the jet array. This discrepancy between the CFD and the experiment (in terms of the bulk movement of the fuel) cannot be definitively explained at this time.

Experimental versus CFD centerline wall pressure traces are shown in Figure 9. Upstream interaction at the centerline is well predicted; however, downstream pressure rise is significantly underpredicted at this point in the CFD. Figure 10 is a plot of the axial distribution of the mixing and combustion efficiencies from the CFD for $\phi = 0.8$, with experimental data points for $\phi = 1.0$ included. The CFD has similar mixing and combustion, as expected from the global-kinetics mechanism. Note that the experimental data indicates extremely high mixing/combustion upstream in the combustor; this is puzzling in light of available contour plots which indicate (as noted earlier) significant fuel-rich region near the duct centerline and significant fuel-lean regions near the duct sidewalls. Work is being done to attempt to understand the experimental data points presented. In any event, far-field combustion efficiencies are similar between experiment and CFD.

2.4 Lessons Learned

A. Wall cooling can result in an increase in the strength of a shock-wave train in a dual-mode isolator, which in turn results in higher pressure levels in the isolator-combustor than observed without cooling. This is believed due primarily to de-energization and thinning of the incoming boundary layer which can: i) facilitate the development of more extensive separation, and ii) result in stronger leading edge oblique shocks due to increased flow turning at the front of the upstream separated zone. The critical importance of 3-D modeling of the upstream-flow is shown clearly by the fact that this relatively small factor can cause subsequent choking of the overall flow, such that the core flow moves from low supersonic (adiabatic walls) to high subsonic (cooled walls).

B. The influence of side-walls in a dual-mode combustor are shown to be very large; the tendency of the interaction zone to move toward the inlet at the side-walls is significant. The assumption of injector-to-injector symmetry in a dual-mode flow-field is a matter of concern. Resource requirements for this already challenging problem are increased significantly by this observation.

C. There is a concern that sonic jets exiting into a highly pressurized combustor (static pressure similar or higher to the exit pressure of the supposedly sonic jet) may disrupt the mass flow-rate expected and result in unexpected lateral variations of fueling which

are not captured by CFD modeling at the current level. This is exacerbated by the three-dimensionality observed across the lateral extent of the isolator-duct.

3.0 Convergence-Acceleration Techniques for Simulation of Dual-Mode Combustors

Simulation of dual-mode scramjet combustors requires the use of a fully-elliptic Navier-Stokes code with finite-rate chemical kinetics and advanced turbulence models. Resource requirements are very high because of the need to simulate side-walls due to inherent three-dimensionality of the dual-mode flow-field, and the low Mach number present in the flow (resulting in small allowable time steps). It is useful to employ convergence-acceleration techniques in order to facilitate faster solution times and minimize resource requirements. Several techniques are discussed below.

i) The transient development of the upstream interaction region can be extraordinarily slow in terms of iterations within a CFD simulation. Essentially, the pressure-driven interaction propagates upstream against the free-stream very reluctantly. It can be advantageous to over-develop the upstream interaction zone initially by the use of artificial techniques; the upstream interaction has been observed to relax back downstream rapidly to the final location. This concept was in fact used by Riggins (1998) with an observed factor of five in terms of convergence acceleration. A number of techniques can be used to develop this over-driven interaction region. Examples include constraining the isolator flow to be laminar, running fast chemistry with upstream fuel injection, and removing the steps (all within the early transients). Another possibility, which has not been tested, is to energize the downstream flow very rapidly via distributed energy sources within the energy equation solver; this would be analogous to pressurizing the flow instantly in order to rapidly establish upstream interaction, rather than waiting for the slow development of pressurization via fuel-air reaction.

ii) Mesh sequencing can be very advantageous (and is predominantly used in this investigation with the code VULCAN). Part of the final upstream interaction can be developed on a coarse grid-sequence with little time requirement.

iii) Combustor-scaling simply reduces the geometry of the rig down to 1/4 scale or less; upstream interaction is developed rapidly in such a sub-scale model (the upstream evolution of the pressurization has much less physical distance to traverse against the main flow). This technique should be used in the early transients and subsequently interpolated (if necessary) into a full-scale solution process. Olynciw et al (1999) indicate that a solution obtained on a sub-scale domain should provide an excellent initial condition for a full-scale simulation.

4.0 Recommendations Regarding Dual-Model Experiment for CFD Validation

This section details a list of desirable features of a dual-mode experiment which would provide an excellent data base for comparing and improving existing numerical techniques. This list is developed from the present base of experience with modeling the dual-mode problem.

Many experiments exist which incorporate some of these features. Unfortunately, the extreme sensitivity of the dual-mode flow-field to turbulence modeling, three-dimensionality, large-scale three-dimensional separation, possible inherent unsteadiness, inflow characteristics, subsonic and supersonic flow, thermal choking, etc., mandates an unusually challenging list of experimental requirements. For instance, an experiment which provides thorough and excellent survey of data in the isolator/combustor but which does not provide complete information on the inflow from the facility-nozzle inlet, would be significantly incomplete from the standpoint of modeling that experiment or even understanding the requirements for modeling. Note also that, due to the three-dimensionality and the coupling with sidewalls (so that upstream interaction could extend well forward along sidewalls), it may be dangerous to design the isolator inlet based on assumed inter-jet symmetry.

Desirable experimental features should include:

- duct-height no greater than 3-4 cm
- low aspect-ratio (1 to 2) cross-section
- moderately-short overall scramjet-length (20-30 duct-heights)
- long isolator (no interaction into facility nozzle)
- rectangular geometry (symmetric top and bottom) with steps
- flush wall-injection, normal to the wall
- circular injectors
- no more than three fuel injectors (two on one surface, the third interdigitated)
- hydrogen as fuel
- high enthalpy (2000 Kelvin) and Mach 2-3 flow at isolator entrance
- no overpressurization at injector exits (jet-to-inflow pressure-ratio greater than 20)
- mass flow-rates and throat pressure measured for each fuel injector

- well-defined inflow, including mass flow-rate and lateral and height surveys of pressure, velocity, temperature, composition (for vitiation), turbulence intensities and length-scales, etc.
- pressure and temperature measurements on side-walls and across top and bottom walls, extending well into facility-nozzle
- flow visualization (Schlierens).

Note that these experimental features are selected with CFD modeling in mind, i.e., they do not necessarily correspond to a desirable rig in an engine.

5.0 Summary

This investigation has focused on the numerical simulation of a specific dual-mode scramjet combustor. Several studies have been undertaken in order to enhance understanding of the ability of CFD to accurately model dual-mode combustors and upstream interaction in isolator ducts. The configuration studied in this work is taken from an experiment conducted in Japan; a number of computational studies of this configuration using three-dimensional Navier-Stokes have been previously reported. Cases examined here include studies with jet-to-jet symmetry (similar to previous numerical studies), entire half-duct modeling, two fuel equivalence-ratio studies, and comparisons with and without wall cooling. Results so far indicate a large sensitivity to wall cooling due primarily to inflow boundary-layer characteristics; large changes in overall flow structure in terms of strength of upstream oblique shock train and subsequent wall pressure values are seen. Very significant lateral displacement of the upstream interaction zone is observed when the entire combustor (half) duct is modeled; this lateral variation cannot be captured with symmetry modeling. The side-walls develop large forward separation bubbles with the greatest extent of upstream interaction occurring at and near the sidewalls. At the high-fuel equivalence-ratios, the upstream interaction was observed to pass into the inlet at the sidewalls. Note that there was no experimental pressure data other than on the centerline of the duct. Experimental fuel contours on downstream planes indicate clustering of fuel toward the centerline of the duct, whereas the CFD indicates fuel moving away from the centerline. Wall pressures for both CFD and experiment indicate that the experimental fuel orifices (nominally assumed sonic) exhaust into a possibly overpressurized environment, thus causing mass flow-rate uncertainties. Studies are continuing on modeling of the half-duct.

An overview of convergence-acceleration techniques useful in the dual mode simulation effort is included. Additionally, desirable characteristics and/or requirements for a well-posed dual-mode experiment useful for CFD comparisons are suggested. The dual-mode environment is very challenging to model and highly-focused experiments are necessary to provide a reliable and unambiguous data base for guiding CFD code improvements.

Acknowledgments

The authors wish to recognize the continuing contribution to this work and related efforts of other members of the mid-speed computational team within the Hyper-X program, including Dr. Taj Mohieldin and Melanie J. Olynciw of Old Dominion University, Dr. Thomas Martin and Marlon Mao of FDC/NYMA Inc., and Jeff White and Charles McClinton of NASA Langley.

References

- Anderson, G.Y. et al (1977), "Experimental Investigation of a Swept-Strut Fuel Injector Concept for Scramjet Applications", NASA TN D-8454, August 1977.
- Billig, F.S. and Dugger, G.L. (1969), "The Interaction of Shock Waves and Heat Addition in the Design of Supersonic Combustors", Proceedings of 12th Symposium on Combustion, Combustion Institute, Pittsburg, PA, 1969, pp. 1125-1134.
- Billig, F.S., Dugger, G.L., and Waltrup, P.J. (1972), "Inlet-Combustor Interface Problems in Scramjet Engines", Proceedings of 1st International Symposium on Airbreathing Engines, Marseilles, France, June 1972.
- Chinzei, N., Komuro, T., Kudou, K., Murakami, A., Tani, K., Masuya, G. and Wakamatsu, Y. (1998), "Effects of Injector Geometry on Scramjet Combustor Performance", AIAA Journal of Propulsion and Power, Vol. 9, No. 1, Jan.-Feb. 1998, pp. 146-152.
- Drummond, J.P., Carpenter, M.H., and Riggins, D.W. (1991), "Mixing and Mixing Enhancement in Supersonic Reaction Flowfields", High-Speed Flight Propulsion Systems, Chapter 7, Progress in Astronautics and Aeronautics, Vol. 137, AIAA, Washington, D.C., 1991.
- Eggers, J.M., Reagon, P.G., and Gooderum, P.B. (1978), "Combustion of Hydrogen in a Two-Dimensional Duct with Step Fuel Injectors", NASA TP-1159, May 1978.
- Komuro, T., Kudo, K., Masuya, G., Chinzei, N., Murakami, A., and Tani, K. (1990), "Experiment on a Rectangular Cross Section Scramjet Combustor" (in Japanese), National Aerospace Lab, NAL TR-1068, Tokyo, Japan, 1990.
- Matsuo, Y., Mizobuchi, Y. and Ogawa, S. (1998), "Parallel Numerical Simulation of Compressible Free Shear Layers in a Scramjet Engine", AIAA Paper 98-0963, January 1998.
- McClinton, C.R. (1978), "Interaction between Step Fuel Injectors on Opposite Walls in a Supersonic Combustor Model", NASA TP-1174, May 1978.
- Menter, F.R. (1992), "Improved Two-Equation $k-\omega$ Turbulence Models for Aerodynamics Flows", NASA TM 103975, October 1992.

- Mizobuchi, Y., Matsuo, Y. and Ogawa, S. (1997), "Numerical Estimation of Turbulence Temperature Fluctuation Effect on Hydrogen-Oxygen Reaction Process", AIAA Paper 97-0910, January 1997.
- Murakami, A., Komuro, T., and Kudo, K. (1993), "Experiment on a Rectangular Cross Section Scramjet Combustor (II) - Effects of Fuel Injector Geometry", (in Japanese), National Aerospace Lab, NAL TR-1220, Tokyo, Japan, 1993.
- Olynciw, M.J., Mohieldin, T.O., McClinton, C.R., and Tiwari, S.N. (1999), "Effects of Scaling on Numerical Modeling of a Transverse Jet into Supersonic Cross Flows", AIAA 99-3368, June 1999.
- Riggins, D.W. (1998), "The Numerical Investigation of a Dual-Mode Scramjet Combustor", 1998 JANNAF Joint Meetings, December 10, 1998.
- Waltrup, P.J. and Billig, F.S. (1973a), "Prediction of Precombustion Wall Pressure Distribution in Scramjet Engines", Journal of Spacecraft and Rockets, Vol. 10, No. 9, 1973, pp. 620-622.
- Waltrup, P.J. and Billig, F.S. (1973b), "Structure of Shock Waves in Cylindrical Ducts", AIAA Journal, Vol. 11, No. 9, 1973, pp. 1404-1408.
- White, J.A. and Morrison, J.H. (1999), "A Pseudo-Temporal Multi-Grid Relaxation Scheme for Solving the Parabolized Navier-Stokes Equations", AIAA 99-3360, June 1999.
- Wilcox, D.C. (1998), *Turbulence Modeling for CFD, 2nd. Edition*, DCW Industries, Inc.

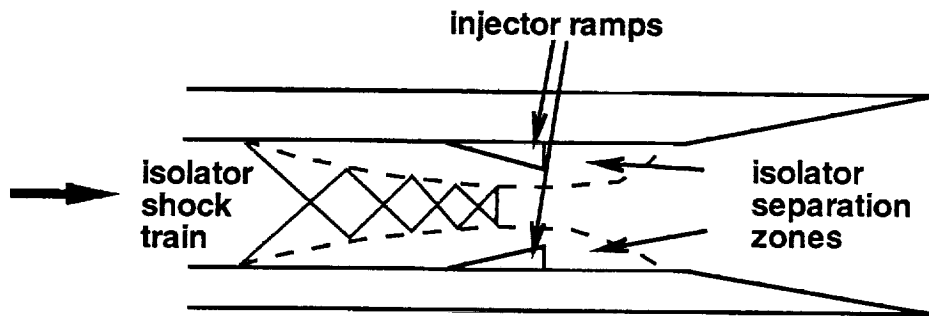


FIGURE 1.

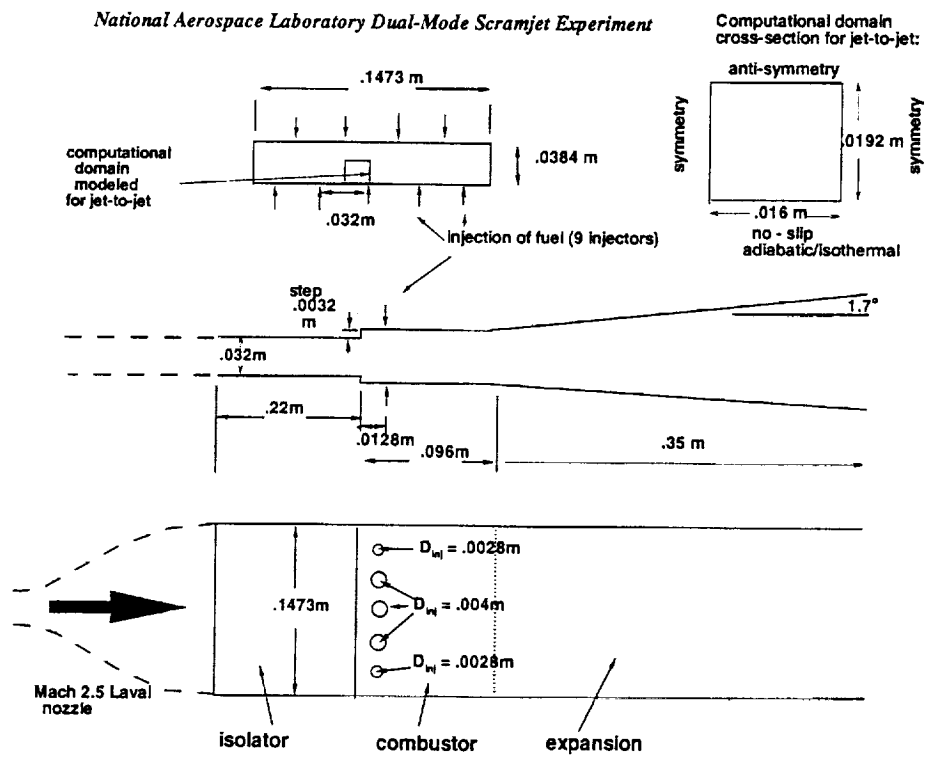


FIGURE 2.

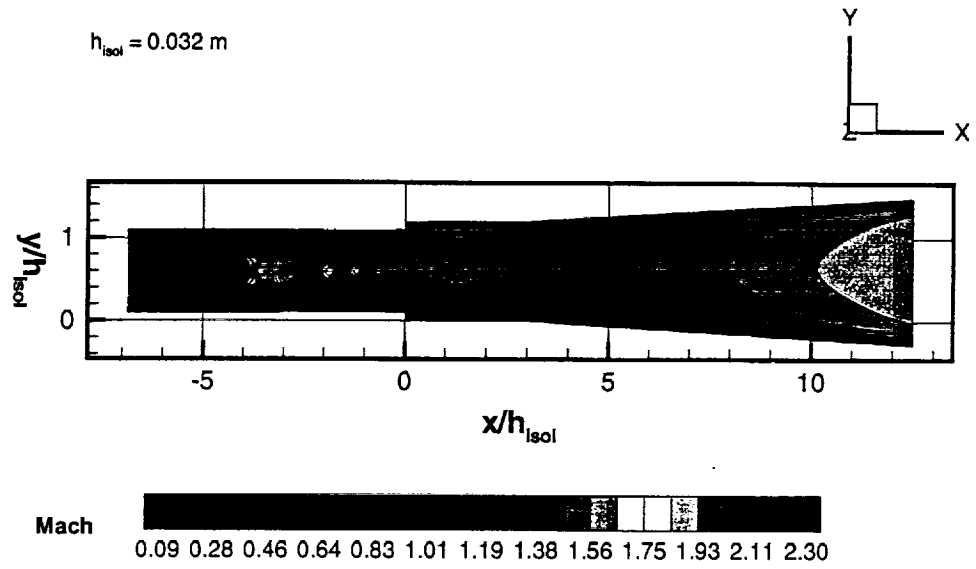


FIGURE 3.

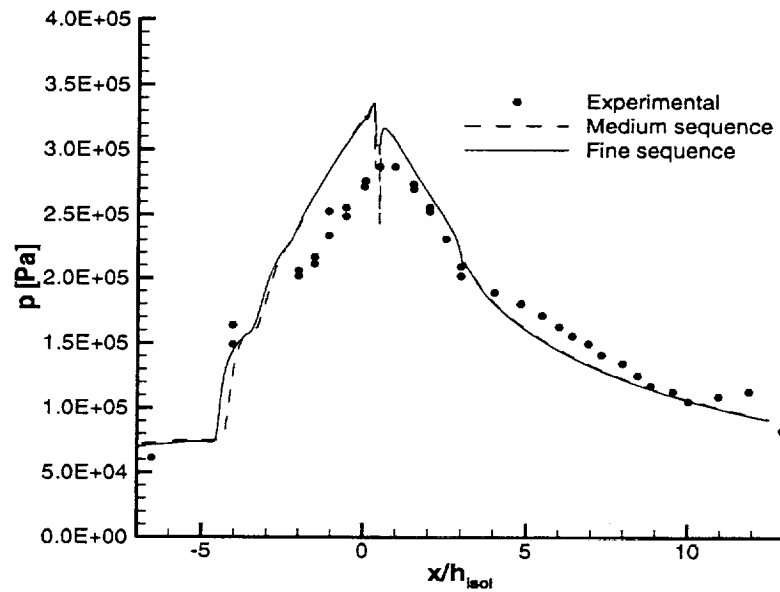


FIGURE 4.

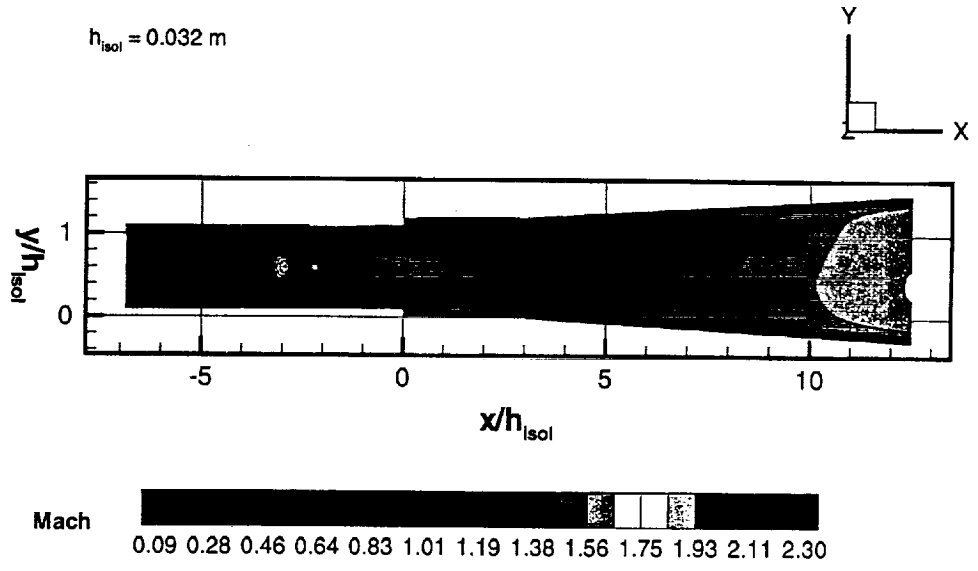


FIGURE 5.

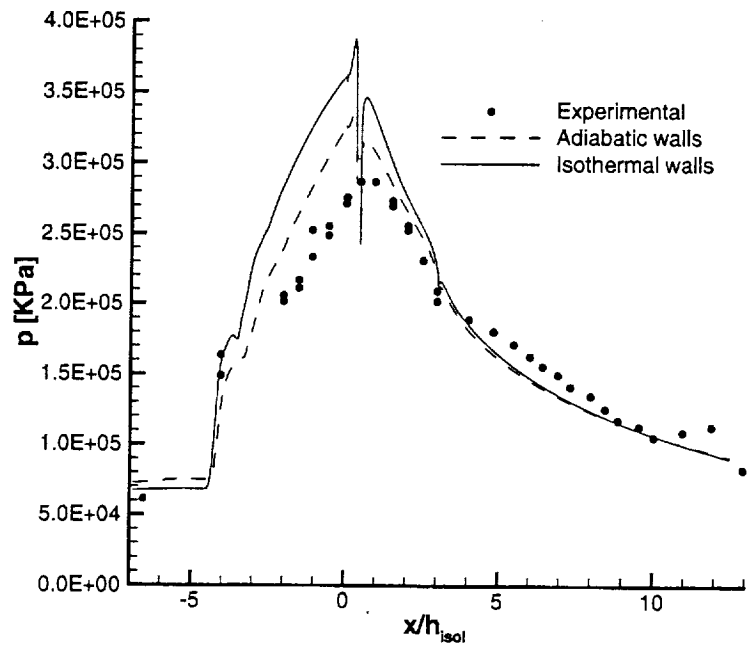


FIGURE 6.

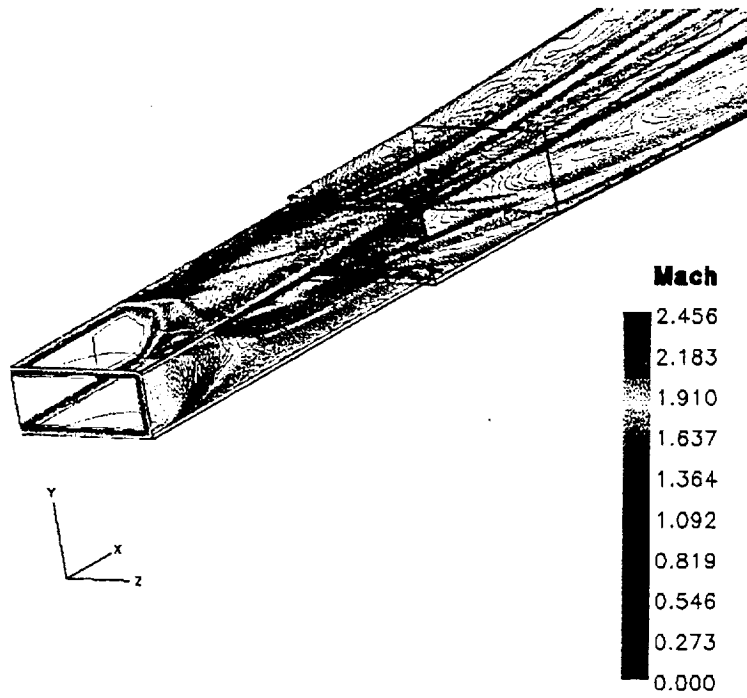


FIGURE 7.

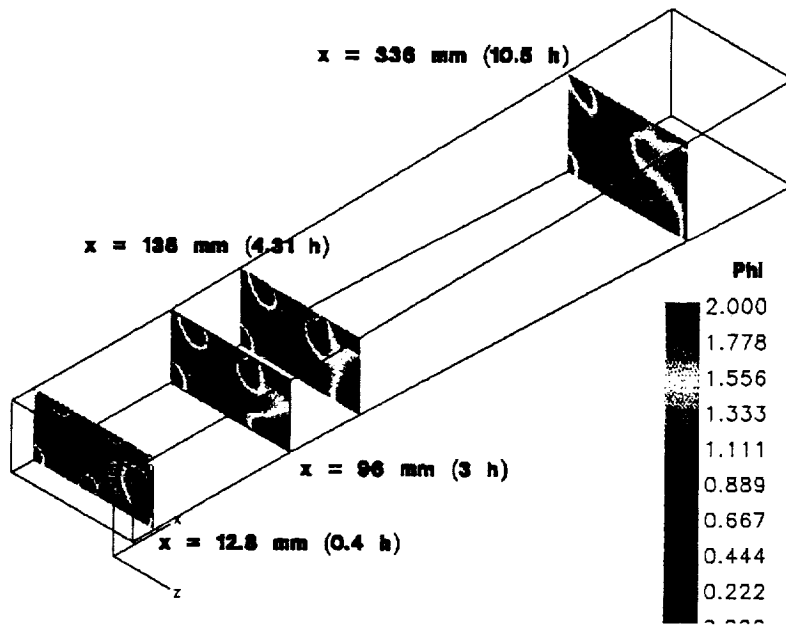


FIGURE 8.

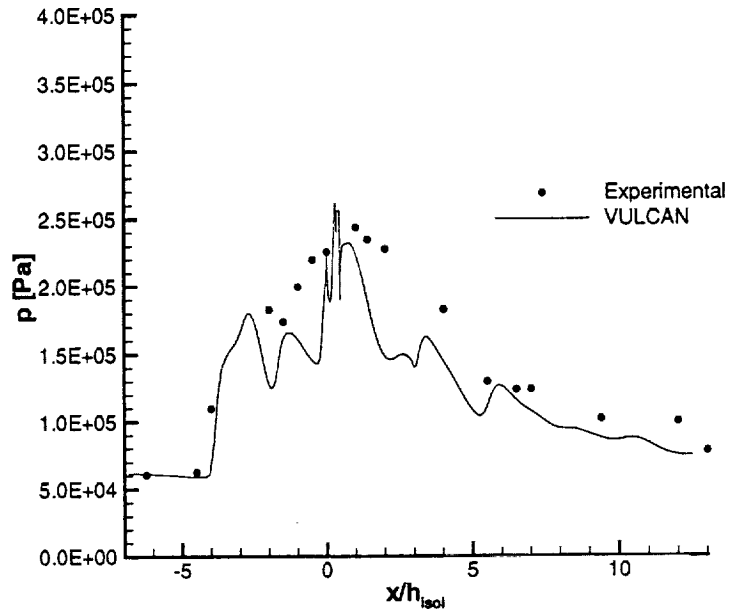


FIGURE 9.

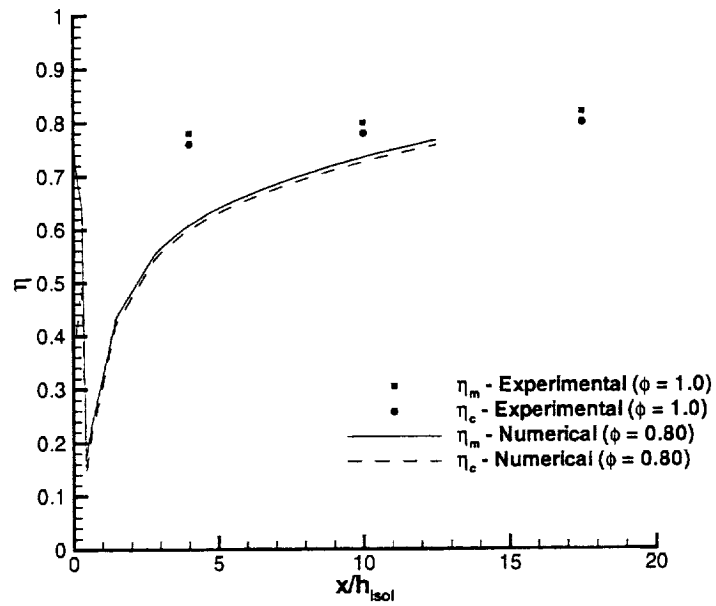


FIGURE 10.



Hypersonic Drag and Heat Transfer Reduction Using a Forward Facing Jet

Benjamin Meyer* and H. F. Nelson†
University of Missouri-Rolla, Rolla MO 65409-0050
and

David W. Riggins‡
University of Tennessee, Knoxville TN 37996-2210

FEL 2⁰ 60

Abstract

A two-dimensional numerical study of the effects of a forward-facing jet located at the stagnation point of a blunt body on wave drag, heat transfer, and skin friction drag is presented for Mach 6.5 flow at 30 km altitude. The full Navier-Stokes equations are used with variable viscosity and thermal conductivity. It is shown that upstream injection can significantly modify the flow field. If the jet conditions are chosen properly, large reductions in drag and heat transfer can be obtained resulting in possible increases in the volumetric efficiency and static stability of aircraft as well as reductions in the heating protection requirements for hypersonic vehicles.

Nomenclature

A_e	= jet exit area per unit width, m ² /m
C_T	= jet thrust coefficient
D	= wave drag per unit width, N/m
d/d_j	= body diameter to jet diameter ratio
d_j	= jet diameter, m
F	= skin friction drag per unit width, N/m
F_N	= nose skin friction drag per unit width, N/m
M_j	= jet exit Mach number
M_∞	= free stream Mach = 6.5
\dot{m}	= mass flow rate, kg/s
P	= pressure, Pa
P_{ij}	= jet total pressure = 375 kPa
P_∞	= free stream total pressure
P_∞	= free stream pressure = 1185.5 Pa
P/P_{i2}	= ratio of pressure to no injection total pressure after main normal shock
q	= dynamic pressure, Pa
Q	= heat transfer rate per unit width, W/m

r	= body nose radius, m
R_D	= wave drag ratio = D/D_{ref}
R_F	= skin friction drag ratio = F/F_{ref}
R_Q	= heat transfer ratio = Q/Q_{ref}
R_Δ	= shock stand-off ratio = Δ/Δ_{ref}
T_j	= jet thrust per unit width, N/m
T_∞	= free stream temperature = 231.24 K
V_e	= jet exit velocity, m/s
Δ	= shock stand-off distance, m
θ	= angle on body, deg.

Introduction

Two major problems in hypersonic flight are large wave drag and surface heating. Both problems can be alleviated by modifying the flow field in front of the body. It is well known that using a structural spike extending from the nose of a blunt body flying at supersonic speeds can significantly reduce drag.¹ A spike has also been shown to reduce the heat transfer to the body surface.² However, the spike becomes hot and ablates due to large stagnation temperatures hence requiring frequent replacement or active cooling. It has been suggested that depositing energy upstream can reduce drag of blunt bodies, e.g. the drag of a cylinder-wedge was reduced by up to 70% using energy deposition.³ However, deposition of energy upstream, in whatever manner accomplished, generally results in increased heat transfer to the surface of the body. Riggins et al.³ stated that there is approximately a 30% increase in heat transfer associated with a 50% drop in external drag using upstream energy deposition. An experimental investigation which employed both a physical spike and energy deposition at the tip of the spike was done by Toro et al.⁴ Several cases were studied: 1) blunt body without a spike, 2) spiked blunt body without tip cooling gas and no energy injection, 3) spiked blunt body with sonic cooling gas from tip and no energy injection, and 4) spiked blunt body with cooling gas and energy injection. It was found that the wave drag decreased sequentially from case 1 to case 4. In a similar study, it was also found that the heat transfer of case 3 was smaller than that of the original blunt body without a spike.⁵

A more desirable method to reduce drag and heat transfer may be to deposit energy in front of the body without using a physical spike. One method for

*Graduate Research Assistant. Student Member AIAA

†Professor of Aerospace Engineering, Thermal Radiative Transfer Group, Department of Mechanical and Aerospace Engineering and Engineering Mechanics. Associate Fellow AIAA

‡Associate Professor of Aerospace Engineering. Senior Member AIAA

Copyright ©1999 by the American Institute of Aeronautics and Astronautics, Inc. All rights reserved.

depositing energy upstream of the body is to inject a combustible mixture, such as a hydrogen-air mixture, from the nose of the body and take advantage of a shock induced combustion reaction. This will result in a large upstream energy release. However, Matsuo et al⁶ showed that upstream combustion results in a large temperature increase along the stagnation streamline behind the bow shock. This inevitably increases heat transfer to the body. However, the use of a non-combustible fluid jet, such as an air jet, will produce a pressure variation on the forebody similar to that observed with a spike⁷, without the heating/structural issues generated by a spike. This paper focuses on the use of inert forward facing jets for obtaining overall drag and heat-transfer reductions on blunt body leading edges at hypersonic velocities.

Charczenko and Hennessey⁷ observed a noticeable decrease in pressure on the nose of a blunt body due to upstream-directed jet thrust. They found that for constant jet thrust the pressure decreases further as the free stream Mach number increases. This means that for constant jet thrust, one expects to see more favorable drag reduction as free stream Mach number is increased. In fact, a study done by Love⁸ at a free-stream Mach number of 1.62, showed that, at this low Mach number, the savings in drag by using a forward facing jet to change the shock layer structure may not be as beneficial as simply placing the jet at the aft of the body because the thrust of the jet exceeds any observed reduction in drag.

A broad investigation by Romeo and Sterrett⁹ found that there are two distinct ways that an upstream-directed jet can affect a blunt body shock. First, at small P_j/P_∞ , the shock is pushed away from the body and does not significantly change in shape. The shock is similar to that which occurs if the blunt body is increased in size. Second, at large ratios of P_j/P_∞ , the shock stand-off distance becomes very large, the jet resembles a spike, and the shock shape changes to resemble that of flow over a body with a sharp leading edge (an oblique shock system forms). The spike is unstable in this second type of flow. These two flow types were also found by Tolle¹⁰ who conducted a study at Mach 14. He found that when the ratio of jet momentum to free stream momentum became greater than 0.1, the flow changed from blunt body flow to spike flow for bodies at zero angle of attack.

The instability of the spike flow exhibits two different forms.^{9,10} The first is a lateral movement in which the shock stays in approximately the same axial location. The second is a cyclic collapse to a blunt body shock. Tolle explains that the collapse is due to the reduced "rigidity" of the longer aerodynamic spike. Small pressure fluctuations on the sides of the aerodynamic spike cause it to move off the axis of symmetry. This, in turn, shortens the spike and the

shock moves closer to the body. Since the spike is now shorter, it centers itself fairly easy and the length of the spike begins to increase, starting the cycle again.

In general, the larger jet thrust required to produce such 'spike' flow results in net increases to the overall drag making the jet counterproductive. Consequently, this study focuses on the blunt body type flow. Specifically, the effects on blunt body overall wave drag, heat transfer, and skin friction drag due to a forward-facing jet are examined by parametrically varying jet exit diameter and exit Mach number while maintaining constant injectant reservoir pressure and temperature.

Computational Methodology

This analysis was done using a modified 2-D version of the time-marching Navier-Stokes code SPARK, which was developed at NASA-Langley Research Center by Drummond¹¹. The full laminar Navier-Stokes equations with variable thermodynamic and diffusion properties as well as variable specific heats are solved in an explicit time marching fashion. The code has the capability to model combustion; however, air was used for injection in this study. Dissociation effects were not considered. All calculations used a constant Prandtl number of 0.7. All cases were run at zero angle of attack and were forced to be symmetrical by imposing symmetry conditions along the stagnation streamline of the body. Thus stability issues of the jet are not investigated. For the no injection and injection cases, 236 by 157 (angular by radial) and 145 by 97 body fitted grids clustered at the body surface were used respectively. The inflow boundary conditions used standard values for an altitude of 30 km: $P_\infty = 1185.5$ Pa, $T_\infty = 231.24$ K. The outflow boundaries used simple extrapolation for all variables. Viscous (no slip) conditions were taken everywhere on the body. Pressure on the body was extrapolated at the local normal. The body surface was maintained at 500 K. Convergence to steady state was based on the achievement of asymptotic values for wave drag, heat transfer, and skin friction drag. For the injection cases, a steady state solution was obtained at approximately 225,000 iterations; however, all cases were run an additional 75,000 iterations to ensure time convergence. Grid and time convergence issues are addressed in appendix A.

Analysis

Two of the important variables for drag studies with upstream injection are shock stand-off distance, Δ , and body diameter to jet diameter ratio, d/d_j . In order to compare results to the reference (no injection) results, a

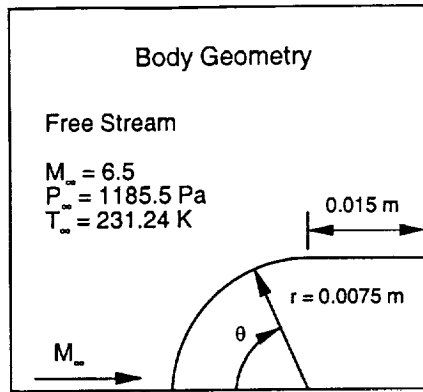


Fig. 1. Body geometry and inlet conditions (half body shown).

ratio, R_i , is defined where i represents variables such as shock stand-off distance, wave drag, heat transfer, and skin friction drag. R_i is defined as the ratio of a variable to the same variable for the reference (no injection) case (e.g. in the case of wave drag: $R_D = D/D_{ref}$). For the case of wave drag, the thrust penalty of the forward-facing jet is included in the overall wave drag value (D). The smaller the value of R_i , the more beneficial the reduction in the variable. When $R_i = 1$ the variable has the same value as that of the no injection case. In the case of R_Q , negative values indicate that the body is being cooled (losing heat). Thus, if the no injection case has a heating rate of 100 W/m , and a given injection case has a value $R_Q = -1$, then the body is cooling at a rate of 100 W/m .

For this analysis the thrust for the forward facing jet is defined as:

$$T_j = \dot{m}V_e + A_e P_e \quad (1)$$

The thrust coefficient is defined as:

$$C_T = \frac{T_j}{q_\infty A} \quad (2)$$

where A is defined as the maximum cross sectional area of the blunt body. It is important to keep in mind throughout this analysis that the jet total pressure and temperature are constant. Thus, for a given exit area, an increase in jet exit Mach number results in a decrease in thrust (see appendix B).

Geometry

Figure 1 shows the blunt body used in this research. The nose radius is 0.0075 m . The analysis is 2-D, hence parameters such as drag are per meter width. The geometry corresponds to the leading edge of a wing. The length of the body in the flow direction, not including the nose, is 0.015 m . Although this length has

no bearing on wave drag calculations (the angle of attack is always zero), it is included in heat transfer and skin friction drag integrations over the surface. The sides of the body are important because if a reattachment shock is present, its effects are not necessarily restricted to the nose region defined by $0 \leq \theta \leq 90 \text{ deg}$. The sides of the body can experience varying temperatures and velocities and thus become important for a complete analysis. The jet is centered at the nose of the body ($\theta = 0$, $r = 0.0075 \text{ m}$) and faces into the free stream. The angle of attack of the body and the jet are fixed at zero.

Comparison to Previous Work

Finley¹² published experimental work in which a jet was injected upstream into Mach 2.5 flow. His investigation covered a range of shapes, d/d_j ratios, and ratios of total jet pressure to after shock total pressure (P_j/P_{t2}). He found that three regimes existed as a function of P_j/P_{t2} . Regime 1, P_j/P_{t2} increasing from 1, was a steady flow with multiple jet cells. As P_j/P_{t2} increased further, there was a small range of P_j/P_{t2} where the flow became unsteady due to the multiple jet cells. Finley calls this range regime 2. Regime 2 ends when a critical ratio of P_j/P_{t2} is reached. For ratios larger than the critical, regime 3, one jet cell existed and the flow was stable.

In order to verify the computational analysis, one of Finley's cases was run. The same computational setup for injection previously mentioned was used, except the incoming conditions were changed to those used by Finley and the body temperature was held at 300 K . Incoming conditions were: $M_\infty = 2.5$, $P_\infty = 275,790 \text{ Pa}$ (40 psia), and $T_\infty = 294 \text{ K}$ ($530 \text{ }^\circ\text{R}$). Jet conditions were: $d/d_j = 9.4$, $M_j = 2.6$, $P_j/P_{t2} = 12$, and $T_{ij} = T_\infty$. The ratio of the jet momentum ($\rho A V_e^2$) to that of the free stream is approximately 0.5. This is much larger than the 0.1 transition point found by Tolle.¹⁰ However, Tolle's work was done at Mach 14. This means that Tolle's P_{t2} was significantly lower than Finley's (Mach 2.5). From this, coupled with the flow stability, one concludes that all of Finley's regimes are of the blunt body flow type. This assumption is confirmed by schlieren photographs from Ref. 12. Finley found that the blunt body flow is stable for regimes 1 and 3. Regime 2, which Finley found unstable, occurs over a very small range of P_j/P_{t2} and would have been difficult to observe in the broad studies of Refs. 8 and 9. Results of the test case are shown in Fig. 2, which shows the ratio of static pressure on the body to total pressure after the shock, P/P_{t2} , as a function of the angle on the body. Finley's experimental results are shown as dashed lines, while the solid lines are the results from the present analysis. The flat region (at approximately

$P/P_{t2} = 0.6, \theta = 0$) is due to the jet. At first glance the injection cases do not appear to correlate very well. However, Finley's experiment was done for a 3-D sphere-cone, while the current results are for a 2-D cylinder-wedge geometry. Examination of shock shape and stand-off relations from Billig¹³ assists in explaining why the pressures on the surface vary between the experimental (3-D) and computational (2-D) results for the injection case of Fig. 2. Billig developed relations for shock stand-off distance for spherical and cylindrical bodies as:

$$\Delta_{\text{sphere}} = \frac{d}{2} 0.143 \exp(3.24/M_{\infty}^2) \quad (3)$$

$$\Delta_{\text{cylinder}} = \frac{d}{2} 0.386 \exp(4.67/M_{\infty}^2) \quad (4)$$

where d is the blunt body diameter and Δ is measured from the nose tip on the stagnation streamline. Equations (3) and (4) give:

$$\frac{\Delta_{\text{cylinder}}}{\Delta_{\text{sphere}}} = 3.393 \quad \text{at } M_{\infty} = 2.5 \quad (5)$$

Thus, Δ for a 2-D cylinder-wedge will be approximately 3.4 times as large as that for a 3-D sphere-cone at $M_{\infty} = 2.5$ due to the relieving effect in the 3-D flow. Since the 2-D case has a larger Δ , the jet can penetrate further upstream resulting in lower pressures on the body surface. The key aspect of this comparison is that the trends of P/P_{t2} from the present analysis agree well with Finley's results. Subsequent results also agree with trends described in Ref. 12.

Results and Discussion

The effect of upstream injection on the wave drag, heat transfer, and skin friction drag are investigated for a 2-D blunt body with a cylindrical nose, flying at Mach 6.5 with ambient conditions at an altitude of 30 km ($P_{\infty} = 1185.5$ Pa, $T_{\infty} = 231.24$ K). A matrix of 15 cases as well as a reference (no injection) case are studied. Three ratios of d/d_j (63.0, 31.5, and 21.0) are used. At each d/d_j , jet exit Mach numbers of 2.0, 2.25, 2.5, 2.75, and 3.0 are considered. Jet exit conditions are calculated from reservoir conditions: $P_{ij} = 375$ kPa and $T_{ij} = 600$ K using standard isentropic flow relations. Thus, given M_j , d_j (equal to area of the jet for 2-D problem), P_{ij} , and T_{ij} , all jet exit conditions are readily determined. This method requires that the throat area change for each case in order to meet the required exit conditions.

Reference Case

Figure 3 shows pressure contours for the no injection case. The shock shape and Δ are shown and agree well

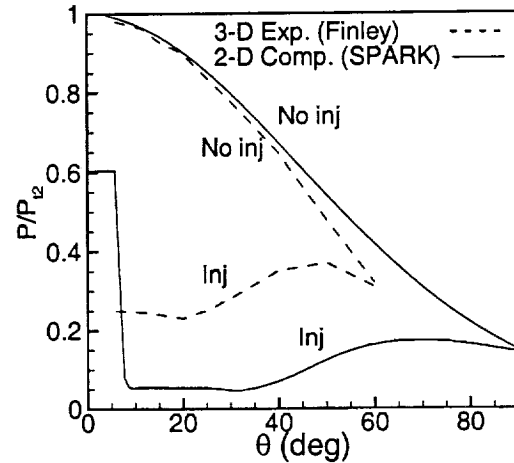


Fig. 2. Comparison of Finley's 3-D experimental and current 2-D computational results. $P_{t2} = 136,942$ Pa.

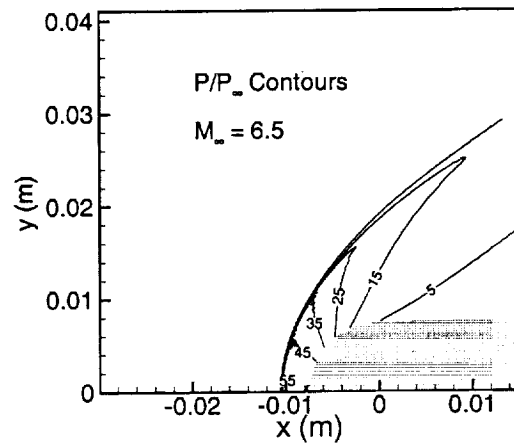


Fig. 3. Nondimensional pressure contours for reference (no injection) case. $P_{\infty} = 1185.5$ Pa.

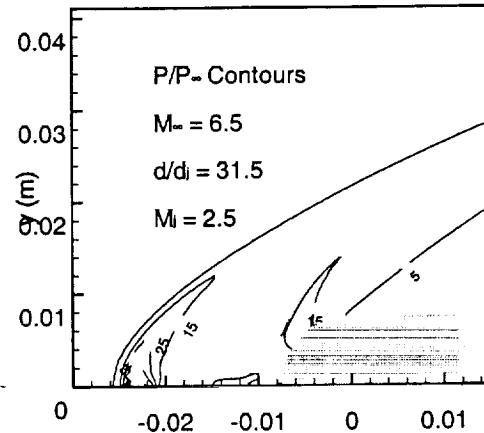


Fig. 4. Nondimensional pressure contours for $d/d_j = 31.5$ and $M_j = 2.5$. $P_{\infty} = 1185.5$ Pa.

with the results of Billig.¹³ The centerline stagnation pressure of 55 times the free stream value also agrees closely with standard shock tables. The no injection, reference values are: $\Delta_{ref} = 0.0030$ m, $D_{ref} = 295.35$ N/m, $Q_{ref} = 10083$ W/m, and $F_{ref} = 5.153$ N/m.

Wave/Jet Drag

Figure 4 shows pressure contours with upstream injection for $d/d_j = 31.5$ and $M_j = 2.5$. For this case, the shock standoff distance has approximately increased by 60% that of the no injection case (i.e. $R_\Delta = 6.10$). This results in significantly lower pressures on the body. The maximum P/P_∞ value is about 20 and occurs near the center of the $P/P_\infty = 15$ contour line on the body. This can also be seen in Fig. 5 which shows P/P_∞ on the nose for $\theta = 0$ to 90 deg for $d/d_j = 31.5$ and $M_j = 2, 2.5,$ and 3 . The no injection curve is also shown for reference. Note that the pressure on the body with injection is generally much less than when there is no injection. Figure 5 shows two key aspects. The first is the large jump in pressure near $\theta = 0$ due to the fixed jet exit pressure which makes a large contribution to the drag and the second is the peak of the P/P_∞ curve which is a function of T_j (or M_j). The lower this peak is and the larger the value of θ at which it occurs, the lower the wave drag is since local wave drag is proportional to $P \cos \theta$. While a P/P_∞ curve may have a very low peak located near 90 degrees indicating a reduction in wave drag, the jet exit pressure also contributes to overall wave/jet drag. In order to move the shock far from the body (pressure peak to large θ) a large jet exit pressure is required. Thus, there is a trade off between the height and position of the peak in Fig. 5 and the jet exit pressure. Figure 5 illustrates how these two key aspects of wave/jet drag work together to change the pressure on the body.

Figure 6 shows R_D (drag reduction) as a function of jet Mach number and d/d_j . Recall that R_D accounts for the reverse thrust of the jet as a contribution to the drag. As M_j is increased, there is a bucket in the drag for $d/d_j = 31.5$ and 21.0 . A bucket would occur for the $d/d_j = 63.0$ case if one extrapolated the curve to lower M_j . Figure 6 clearly shows that for a given d/d_j and free stream condition, there are optimum jet conditions to minimize the drag. If the jet thrust is too small (large M_j) the jet is not being used to its fullest potential to move the shock away from the body. However, if the jet thrust is too large (small M_j), the upstream thrust created by the jet alone will contribute to the overall drag, increasing R_D . The minimum values are as low as 45% of the no-injection case.

There are three main factors which affect the drag: 1) thrust of the jet, 2) Δ , which is affected by the jet thrust, and 3) diameter ratio, d/d_j . As shown previously by

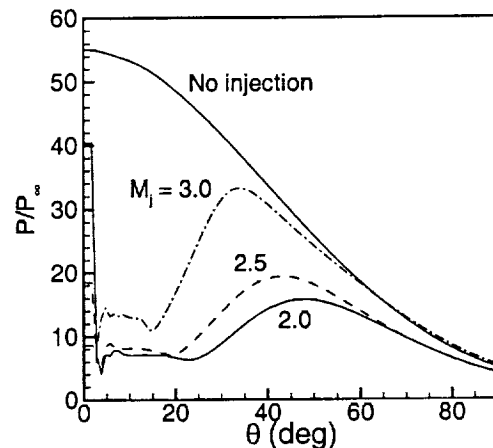


Fig. 5. Nondimensional pressure distribution on blunt body nose for $d/d_j = 31.5$. $P_\infty = 1185.5$ Pa.

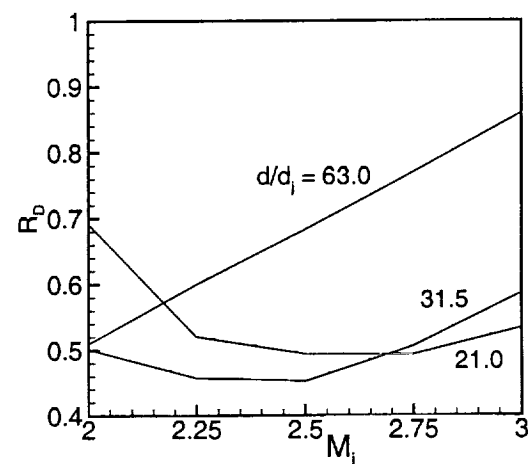


Fig. 6. Drag ratio as a function of jet Mach number. $D_{ref} = 295.35$ N/m

Figs. 3 and 4, the larger the Δ , the lower the value of the maximum pressure ratio on the body. To reduce the drag, the reattachment point also must be moved as far aft on the body as possible. Moving the attachment point shifts the peak of the curves in Fig. 5 as discussed earlier. The importance of d/d_j in this respect is now examined. From Fig. 7 it is clear that the center of vorticity is at approximately $y = 0.0016$ m and a reattachment point exists at $y = 0.0038$ m (or $\theta = 30^\circ$). Figure 8 shows the same area on the body at the same M_j with d/d_j one third that of Fig. 7. Note that the center of vorticity has moved to approximately $y = 0.0026$ m and the reattachment point is now at $y = 0.0051$ m (or $\theta = 43^\circ$). Thus, at smaller d/d_j , the reattachment point moves further aft (larger θ on Fig. 1), and therefore the pressure drag component is reduced. Figure 9 clarifies

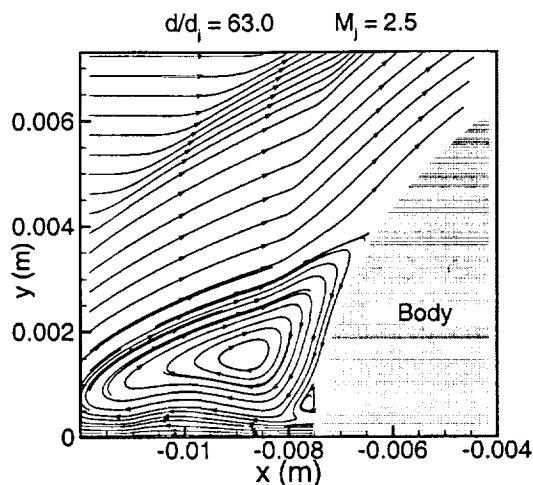


Fig. 7. Close up view of streamlines showing reattachment point for largest d/d_j , 63.0.

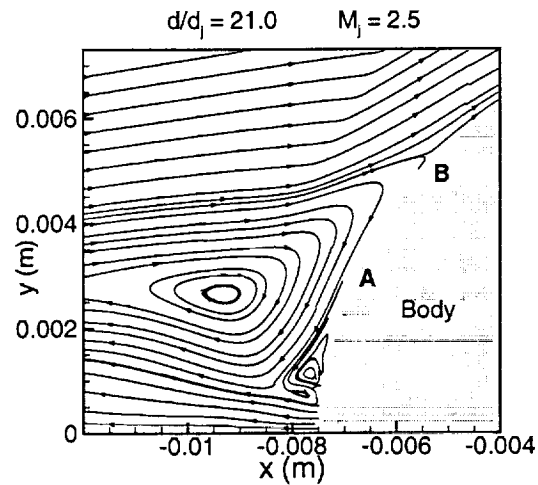


Fig. 8. Close up view of streamlines showing reattachment point for smallest d/d_j , 21.0.

this point. This figure shows P/P_{∞} on the body for $M_j = 2.5$ with varying d/d_j . The no injection case is also shown. Note that the peak of each curve moves to larger values of θ (further aft on the body) as d/d_j is reduced (the height of the peaks are dependent on Δ which is dependent on C_T). From Figs. 7 and 8 the angles of the reattachment points can be calculated as approximately $\theta = 30^\circ$ and 43° respectively. By comparing these values to the same cases on Fig. 9, it is seen that the maximum pressure ratio occurs slightly aft of the reattachment point. Thus, as the reattachment point moves aft on the body, the peak of the curve shifts to larger values of θ , and the wave drag decreases since drag is proportional to $P \cos \theta$. This analysis has examined three main related parameters which control wave/jet drag reductions: d/d_j , Δ , and T_j . The two latter of these parameters are directly dependent on C_T . Careful choice of these three parameters can lead to significant drag reduction as shown in Table 1 which shows R_D as a function of d/d_j and M_j .

Table 1 R_D as a function of d/d_j and M_j
 $D_{ref} = 295.35 \text{ N/m}$

d/d_j	M_j				
	2.00	2.25	2.50	2.75	3.00
63.0	0.509	0.600	0.682	0.770	0.859
31.5	0.501	0.457	0.452	0.505	0.586
21.0	0.691	0.520	0.493	0.493	0.533

Heat Transfer Rate

The heat transfer rate is calculated from the stagnation point to the end of the body, $x = 0.015 \text{ m}$, in order to study the heating/cooling effects of forward-facing injection. The main parameters controlling heat transfer

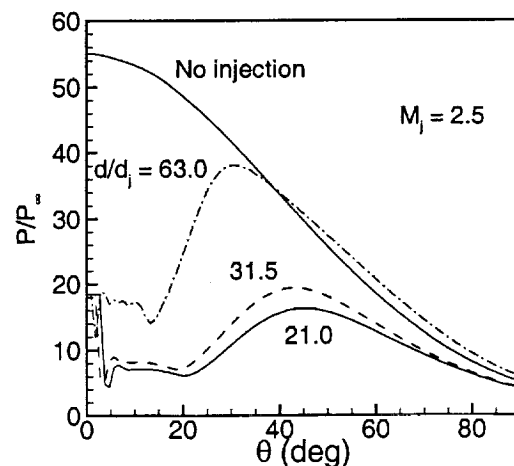


Fig. 9. Nondimensional Pressure distribution on blunt body nose for $M_j = 2.5$. $P_{\infty} = 1185.5 \text{ Pa}$.

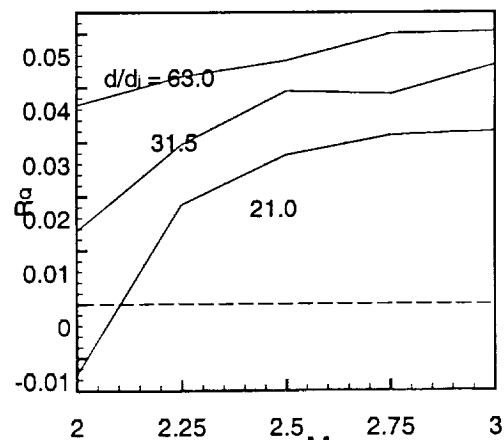


Fig. 10. Heat transfer rate as a function of jet exit Mach number. $Q_{ref} = 10083 \text{ W/m}$.

to the body are the same as those that control drag. Figure 10 shows R_Q (heat transfer normalized by the reference no-injection heat transfer) as a function of M_j for three values of d/d_j . Note that as the M_j increases for a constant value of d/d_j , Q increases. It must be remembered that the jet total pressure and total temperature are the same for all cases. Thus, as M_j increases, the jet thrust decreases, which decreases Δ . This relationship between jet thrust (or C_T) and Δ (or R_Δ) can be seen in Fig. 11. Note that R_Δ increases as C_T increases. The rate of increase becomes smaller as C_T becomes large, indicating that R_Δ will reach a limiting value for large thrust coefficients. It is important to note however that for the cases in this study, an increase in C_T (reduction in M_j) corresponds to an increase in R_Δ (or Δ) for all values of C_T (except for one point as seen in Fig 11). As the shock moves away from the body, the thickness of the layer of jet air washing over the body increases. Since the fluid is exhausted at relatively cool temperatures, the thicker fluid layer reduces the heat transfer to the body. Figure 12 shows injectant air contours for $M_j = 2$ and 3 at $d/d_j = 31.5$. The air injected at $M_j = 2$ in Fig. 12 is very cool compared to the body. In fact, if the jet penetrates upstream even further, as in the $M_j = 2.0$, $d/d_j = 63.0$ case, the air flow actually cools the flow around the body at 1.31% of the heat transfer rate for the no injection case, i.e. $R_Q = -0.0131$ as shown in Fig. 10. For the $M_j = 3$ case in Fig. 12, the body is being heated at a rate of 4.42% of the no-injection case, i.e. $R_Q = 0.0442$ on Fig. 10. When the injected fluid penetrates further upstream (larger Δ) it also expands more due to the region of low pressure air recirculating in the jet near the body seen in Figs. 7 and 8. This expansion creates a thicker boundary layer and thus decreases heating. Figure 13 shows the importance of Δ (which directly affects the fluid thickness over the body). From this figure an inverse relationship between R_Q and R_Δ can be seen. This figure suggests that the major factor in heat transfer to the body is Δ . Table 2 gives numerical values for R_Q as a function of d/d_j and M_j .

Table 2 R_Q as a function of d/d_j and M_j ,
 $Q_{ref} = 10083 \text{ W/m}$

d/d_j	M_j				
	2.00	2.25	2.50	2.75	3.00
63.0	0.0368	0.0420	0.0450	0.0500	0.0504
31.5	0.0136	0.0296	0.0393	0.0388	0.0442
21.0	-0.0130	0.0185	0.0276	0.0312	0.0325

Skin Friction Drag

Leading edge skin friction drag is usually dominated by wave drag at hypersonic velocities; however, it is still of interest to see how it is affected due to upstream

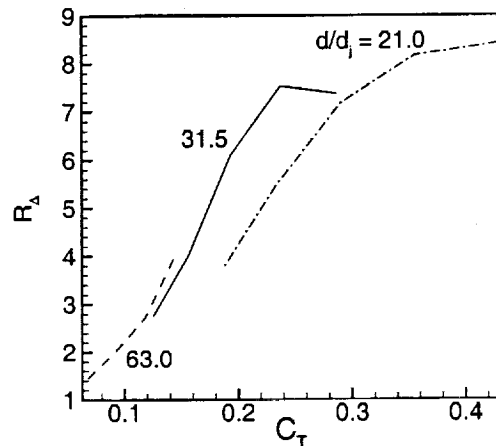


Fig. 11. R_Δ as a function of jet thrust coefficient. $\Delta_{ref} = 0.0035 \text{ m}$.

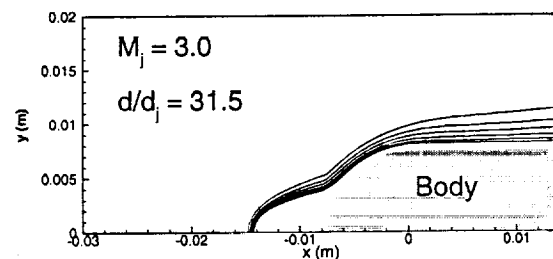
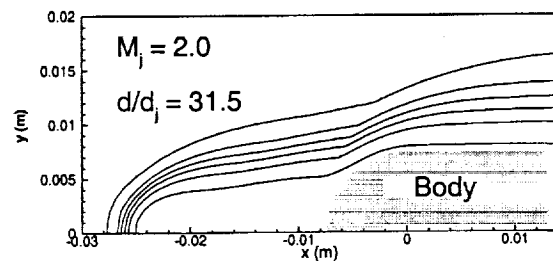


Fig. 12. Jet fluid contours showing injectant thickness over body for jet Mach number of 2.0 and 3.0 with $d/d_j = 31.5$.

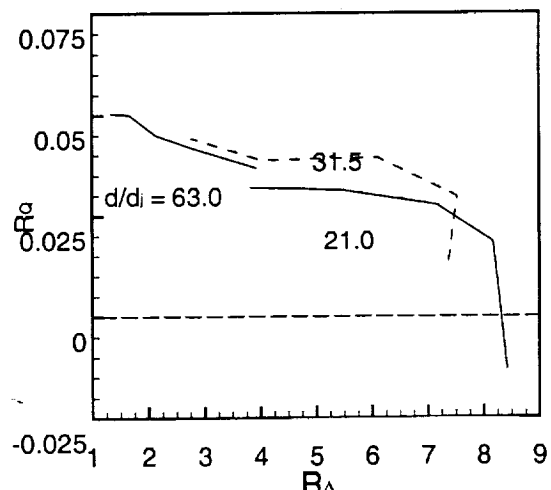


Fig. 13. Heat transfer rate as a function of shock stand-off ratio. $Q_{ref} = 10083 \text{ W/m}$. $\Delta_{ref} = 0.0030 \text{ m}$.

injection. The recirculation zone is largely responsible for skin friction drag reduction. The recirculation causes the flow to move upstream along the body which causes a decrease in the total skin friction drag (Figs. 7 and 8 show the recirculation zone). As the size of the recirculation zone increases, more of the body experiences reverse shear (upstream) due to the recirculating fluid. Figure 14 shows this effect clearly. The no-injection case is shown for reference. The local skin friction drag is nondimensionalized by the value of local skin friction drag for the no injection case at $\theta = 90^\circ$, $F_{ref}(90)$. Figure 14 shows that as d/d_j decreases (increasing the size of the recirculation region) the bucket in the $F(\theta)/F_{ref}(90)$ curve becomes deeper (more negative) and moves to larger values of θ . This indicates that the reattachment point is moving aft on the body and the size of the recirculation zone is increasing. The bucket in the curves is located on the body near the midpoint between the jet and the reattachment point. This is shown as region A in Fig. 8 and corresponds to where the reverse velocity near the body is highest. From Fig. 14 it can be seen that the local skin friction drag passes through the $F(\theta)/F_{ref}(90) = 0$ at the reattachment point. This is shown as region B on Fig. 8. As the flow reattaches and begins to move downstream, the skin friction drag becomes positive. Thus, the larger this recirculation region, the more of a given curve in Fig. 14 will be below the $F(\theta)/F_{ref}(90) = 0$ line thus resulting in lower total skin friction drag. If upstream injection is present, a reduction in skin friction drag is expected because there will always be a recirculation zone. The total skin friction drag on the nose, F_N , may be calculated using the data from Fig. 14. Since Fig. 14 presents the local skin friction drag as a function of the angle on the body, the drag on the nose of the body due to skin friction can be calculated from Eq. (6):

$$F_N = F_{ref}(90) \int_0^{90} \frac{F(\theta)}{F_{ref}(90)} d\theta \quad (6)$$

By including the skin friction from $x = 0$ to 0.015 in Eq. (6) (which is $\theta > 90$ deg., not shown in Fig. 14), the total skin friction drag, F , may be found. Figure 15 shows the skin friction drag as a function of M_j for specific values of d/d_j . As stated above, smaller values of d/d_j yield lower values of R_F . For a given d/d_j , the skin friction drag increases as M_j increases. This occurs because the jet thrust is decreasing, decreasing Δ , which decreases the size of the recirculation region, moving the reattachment point to smaller θ , which causes an increase in the total skin friction drag. Table 3 gives numerical values for R_F as a function of d/d_j and M_j .

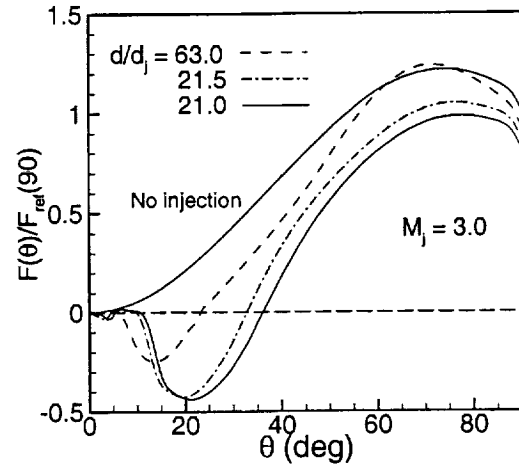


Fig. 14. Nondimensional local skin friction drag as a function of angle on body nose for $M_j = 3.0$. $F_{ref}(90) = 0.02547$ N/m.

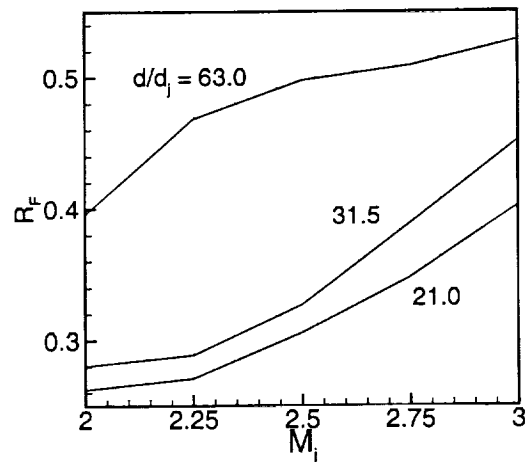


Fig. 15. Nondimensional skin friction drag as a function of jet Mach number. $F_{ref} = 5.153$ N/m

Table 3 R_F as a function of d/d_j and M_j
 $F_{ref} = 5.153$ N/m

d/d_j	M_j				
	2.00	2.25	2.50	2.75	3.00
63.0	0.396	0.468	0.498	0.509	0.529
31.5	0.280	0.289	0.327	0.389	0.452
21.0	0.262	0.271	0.306	0.348	0.403

Conclusions

The effects of a supersonic jet injecting upstream from the stagnation point of a blunt body flying at Mach 6.5 at 30 km altitude are investigated. Specifically, wave

drag, heat transfer, and skin friction drag on the leading edge of the body are examined. The injection is shown to significantly modify the flow field. Wave drag including the drag penalty of the forward-facing jet is shown to reduce by as much as 45%. Heat transfer rates can be dramatically reduced and can actually reverse, i.e. the flow along the body surface cools the flow around the body in the leading edge region. Skin friction drag is also shown to decrease due to upstream injection. The primary mechanisms controlling wave drag and skin friction drag are found to be shock stand-off distance and the ratio of body diameter to jet diameter. The heat transfer rate is governed primarily by the shock stand-off distance. By using proper jet exit conditions, the wave drag, heat transfer rate, and skin friction drag can be significantly reduced. Larger blunt body noses which allow for the inclusion of injectors can use forward jet(s) to reduce and even eliminate thermal loads while simultaneously reducing the drag of hypersonic leading edges.

Acknowledgments

This research has been partially funded by NASA NAG-1-2167 grant from the HYPER-X Program Office, C. R. McClinton, Technical Monitor, NASA Langley Research Center, Hampton, VA.

References

¹Hutt, C. R. and Howe, A. J., "Forward Facing Spike Effects of Bodies of Different Cross Section in Supersonic Flow," *The Aeronautical Journal of the Royal Aeronautical Society*, June/July 1989, pp. 229-234.

²Yamauchi, M., Fujii, K., and Higashino, F., "Numerical Investigation of Supersonic Flows Around a Spiked Blunt Body," *Journal of Spacecraft and Rockets*, Vol. 32, No. 1, 1995, pp. 32-42.

³Riggins, D. W., Nelson, H. F., and Johnson, E., "Blunt Body Wave Drag Reduction Using Focused Energy Deposition," *AIAA Journal*, Vol. 37, No. 4, 1998, pp. 460-504.

⁴Toro, P. G.P., Nagamatsu, H. T., Minucci, M. A.S., and Myrabo, L. N., "Experimental Pressure Investigation of a 'Directed-Energy Air Spike' Inlet at Mach 10," AIAA Paper 99-2843, June 1999.

⁵Toro, P. G.P., Nagamatsu, H. T., Myrabo, L. N., and Minucci, M. A.S., "Experimental Heat Transfer Investigation of a 'Directed-Energy Air Spike' Inlet at Mach 10," AIAA Paper 99-2844, June 1999.

⁶Matsuo, A., Fujii, K., and Fujiwara, T., "Flow Features of Shock-Induced Combustion Around Projectile Traveling at Hypervelocities," *AIAA Journal*, Vol. 33, No. 6, 1995, pp. 1056-1063.

⁷Charczenko, N. and Hennessey, K. W., "Investigation of a Retrorocket Exhausting From the Nose of a Blunt Body into a Supersonic Free Stream," NASA Technical Note D-751, Sept. 1961.

⁸Love, E. S., "The Effects of a Small Jet of Air Exhausting From the Nose of a Body of Revolution in Supersonic Flow," NACA Research Memorandum L52II9a, Nov 12, 1952.

⁹Romeo, D. J. and Sterrett, J. R., "Exploratory Investigation of the Effect of a Forward-Facing Jet on the Bow Shock of a Blunt Body in a Mach 6 Free Stream," NASA Technical Note D-1605, Feb 1963.

¹⁰Tolle, F. F., "An Investigation of the Influence of a Forward Ejected Gas Stream on Hypersonic Flow about Blunt Bodies," Dissertation at the University of Arizona, 1973.

¹¹Drummond, J. P., Rogers, R. C., and Hussaini, M. Y., "A Detailed Numerical Model of a Supersonic Mixing Layer," AIAA Paper 86-1427, June 1986

¹²Finley, J. P., "The Flow of a Jet From a Body Opposing a Supersonic Free Stream," *Journal of Fluid Mechanics*, Vol. 26, part 2, Oct. 1966, pp. 337-368.

¹³Billig, F. S., "Shock Wave Shapes Around Spherical- and Cylindrical-Nosed Bodies," *Journal of Spacecraft and Rockets*, Vol. 4, June 1967, pp. 822-823.

Appendix A. Convergence

An intensive grid and time convergence study was undertaken. 3 grids were used for both the injection and no injection case. Each successive grid increased the number of points in the boundary layer at least two fold. For time convergence, the number of iterations was increased by increments of 75,000 until steady state was reached. When all three grids reached steady state convergence, they were compared to each other for grid convergence. Table A1 shows the percent change for wave drag, heat transfer, and skin friction drag for time and grid convergence for the injection and no injection cases. Note that all values are converged to at least 10%, with most converging to at least 5%.

Table A1 Grid and time convergence

	Injection		No Injection	
	Time	Grid	Time	Grid
Wave drag	0.25%	2.12%	0.00%	0.00%
Heat transfer	1.56%	5.97%	0.02%	9.75%
Skin friction	0.99%	10.4%	0.02%	4.24%

Appendix B. Thrust and Mach Relationship

This section shows the inverse relationship between jet Mach number and jet thrust with constant total pressure and temperature and with constant jet exit area (note

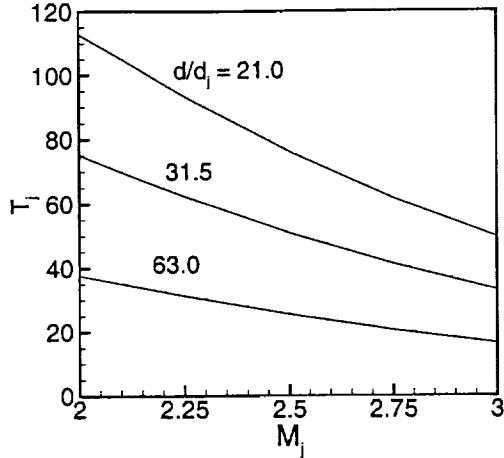


Fig. 16. Jet thrust as a function of jet Mach number

that throat area changes to meet required conditions). The first step is to write the equation for thrust:

$$T_j = \dot{m}V_e + A_e P_e \quad (A1)$$

Eq. (A1) can be rewritten as:

$$T_j = A_e P_e (\gamma M_j^2 + 1) \quad (A2)$$

with $\gamma = 1.4$. Differentiating Eq. (A2) with respect to M_j yields:

$$\frac{\partial T_j}{\partial M_j} = A_e P_e (2\gamma M_j) + A_e (\gamma M_j^2 + 1) \frac{\partial P_e}{\partial M_j} \quad (A3)$$

By differentiating the following equation for P_{ij} (constant) with respect to M_j :

$$P_{ij} = P_e \left(1 + \frac{\gamma - 1}{2} M_j^2\right)^{\frac{\gamma}{\gamma - 1}} \quad (A4)$$

one can solve for $\partial P_e / \partial M_j$ and obtain:

$$\frac{\partial P_e}{\partial M_j} = \frac{-\gamma P_e M_j}{1 + \frac{\gamma - 1}{2} M_j^2} \quad (A5)$$

Equation (A5) can then be substituted into Eq. (A3) to obtain:

$$\frac{\partial T_j}{\partial M_j} = 2\gamma A_e M_j P_e \left(\frac{1 - M_j^2}{2 + (\gamma - 1)M_j^2} \right) \quad (A6)$$

Note that all the variables in Eq. (A6) are positive. Thus, from the numerator term in the parentheses, if M_j is greater than one (which is always the case for this study) the change in thrust with respect to jet Mach number will be negative. Therefore, as the jet Mach number increases, the jet thrust will decrease. This can also be seen by solving Eq. (A4) for P_e and substituting into Eq. (A2) to obtain:

$$T_j = A_e P_{ij} \frac{(\gamma M_j^2 + 1)}{\left(1 + \frac{\gamma - 1}{2} M_j^2\right)^{\frac{\gamma}{\gamma - 1}}} \quad (A7)$$

Since A_e and P_{ij} are constant, one sees from Eq. (A7) that the denominator will dominate as M_j is increased, decreasing T_j . Figure 16 shows the relationship between the thrust and Mach number of the jet. Note that, as shown by Eqs. (A6) and (A7), as the jet Mach number increases, the jet thrust decreases. The different slopes in the curves are due to the different exit areas. From Eq. (A4), one notes that with γ and P_{ij} constant, P_e will have the same value for all curves in Fig. 16 for a given M_j . For given P_e , M_j , and γ , the slopes of the curves ($\partial T_j / \partial M_j$) are governed by A_e as shown by Eq. (A6). As A_e increases, d/d_j decreases. Thus, for the smallest d/d_j , $\partial T_j / \partial M_j$ has the largest negative value.